The D/H ratio in Titan's acetylene from high spectral resolution IRTF/TEXES observations

B. Bézard, C.A. Nixon, S. Vinatier, E. Lellouch, T. Greathouse, R. Giles, N.A. Lombardo, A. Jolly

Research Paper

The D/H ratio in Titan's acetylene from high spectral resolution IRTF/TEXES observations

B. Bézard [a],[*], C.A. Nixon [b], S. Vinatier [a], E. Lellouch [a], T. Greathouse [c],[1], R. Giles [c], N.A. Lombardo [b],[2], A. Jolly [d]

[a] LESIA, Observatoire de Paris, Université PSL, Sorbonne Université, Université Paris Cité, CNRS, Place Jules Janssen, Meudon 92195, France
[b] NASA Goddard Space Flight Center, Greenbelt, 20771, MD, United States
[c] Southwest Research Institute, San Antonio TX, United States
[d] LISA, CNRS UMR 7583, Université Paris-Est Créteil, Université Paris-Cité, IPSL, Créteil 94010, France

ARTICLE INFO

ABSTRACT

We report observations of deuterated acetylene (C_2HD) at 19.3 μm (519 cm^{-1}) with the Texas Echelon Cross Echelle Spectrograph on the NASA Infrared Telescope Facility in July 2017. Six individual lines from the Q-branch of the v_4 band were clearly detected with a S/N ratio up to 10. Spectral intervals around 8.0 μm (745 cm^{-1}) and 13.4 μm (1247 cm^{-1}) containing acetylene (C_2H_2) and methane (CH_4) lines respectively, were observed during the same run to constrain the disk-averaged C_2H_2 abundance profile and temperature profile. *Cassini* observations with the Composite Infrared Spectrometer (CIRS) were used to improve the flux calibration and help to constrain the atmospheric model. The measured D/H ratio in acetylene, derived from the C_2HD/C_2H_2 abundance ratio, is $(1.22^{+0.27}_{-0.21}) \times 10^{-4}$, consistent with that in methane obtained in previous studies. Possible sources of fractionation at different steps of the acetylene photochemistry are investigated.

1. Introduction

Titan's complex photochemistry produces a suite of hydrocarbons and nitrogen-bearing compounds, eventually leading to the formation of haze particles. This chemistry is initiated by the dissociation and ionization of dinitrogen (N_2) and methane (CH_4) by ultraviolet solar radiation, particles from Saturn's magnetosphere and galactic cosmic rays. The vertical and horizontal abundance profiles of many of these photochemical species along with their seasonal variations have been extensively characterized through Cassini observations (e.g. Coustenis et al., 2020; Mathé et al., 2020; Tribbett et al., 2021; Vinatier et al., 2020, for the most recent ones). These investigations are complemented by other space-based and ground-based millimeter and mid-infrared observations, which in particular allowed the detections of new photochemical compounds (Lombardo et al., 2019; Moreno et al., 2011; Nixon et al., 2020; Thelen et al., 2020).

Observational data serve as constraints for photochemical models that aim at understanding the chemistry at work in Titan's atmosphere (e.g. Moreno et al., 2012; Dobrijevic et al., 2014; Krasnopolsky, 2014; Dobrijevic et al., 2016; Lara et al., 2014; Vuitton et al., 2019). Besides chemical abundance profiles, isotopic ratios may provide valuable information on the chemical and physical processes involved in the production and loss of the species. For example, the large difference in the $^{14}N/^{15}N$ ratio observed in HCN (Marten et al., 2002; Gurwell, 2004; Vinatier et al., 2007b; Courtin et al., 2011) and in N_2 (Niemann et al., 2010), the main nitrogen reservoir, allows us to constrain the relative flux of fractionated N atoms from photolysis and non-fractionated N atoms from other processes, such as magnetospheric electrons or galactic cosmic rays (Dobrijevic and Loison, 2018; Vuitton et al., 2019).

Dissociation of methane by solar ultraviolet radiation is the primary source of the hydrocarbons produced on Titan. Methane is also lost by reactions with various photochemical products and, most importantly, by reaction with the C_2H radical below 600 km. These processes are

---

* Corresponding author.
E-mail addresses: bruno.bezard@obspm.fr (B. Bézard), conor.a.nixon@nasa.gov (C.A. Nixon), sandrine.vinatier@obspm.fr (S. Vinatier), emmanuel.lellouch@obspm.fr (E. Lellouch), thomas.greathouse@swri.org (T. Greathouse), rohini.giles@swri.org (R. Giles), nicholas.lombardo@yale.edu (N.A. Lombardo), jolly@lisa.ipsl.fr (A. Jolly).
[1] Visiting Astronomer at the Infrared Telescope Facility, which is operated by the University of Hawaii under contract 80HQTR19D0030 with the National Aeronautics and Space Administration.
[2] Present address: Department of Earth and Planetary Sciences, Yale University, New Heaven, CT 06511, United States.

Table 1
TEXES observations of Titan.

Target molecule	Date (UT)	Spectral interval (cm^{-1})	Spectral resolution (cm^{-1})	Titan–Earth distance (AU)	Slit width (arcsec)	Integration time (s)	Maximum S/N (per spectel)
C$_2$HD	July 8, 2017	518.4–520.0	0.0077	9.124	2.0	910	15
C$_2$H$_2$	July 14, 2017	742.9–746.7	0.0078	9.163	1.4	830	50
CH$_4$	July 8, 2017	1244.3–1250.7	0.0156	9.124	1.4	770	20

potentially a source of hydrogen fractionation in the photochemical products as they preferentially break the C–H bond over the stronger C–D bond (Pinto et al., 1986; Lunine et al., 1999). Thus measuring the D/H ratio in various hydrocarbons can shed light on different photochemical pathways at work on Titan.

Besides methane, the only hydrocarbon in which the D/H ratio has been measured is acetylene (C$_2$H$_2$). Fitting simultaneously the 14.7-μm (678 cm^{-1}) ν_5 band of C$_2$HD and the nearby 13.7-μm (729 cm^{-1}) ν_5 band of C$_2$H$_2$ observed in spectral averages of nadir Cassini/CIRS spectra, Coustenis et al. (2008) inferred a D/H ratio in C$_2$H$_2$ of (2.09 ± 0.45) × 10^{-4}. This ratio appears significantly larger than that in methane, which is in the range (1.1–1.6) × 10^{-4} (Owen et al., 1986; de Bergh et al., 1988; Coustenis et al., 1989, 2003; Penteado et al., 2005; Bézard et al., 2007; Coustenis et al., 2007; Abbas et al., 2010; de Bergh et al., 2012; Nixon et al., 2012). However, from the analysis of CIRS limb spectra, Coustenis et al. (2008) derived a lower value of the D/H ratio in C$_2$H$_2$, (1.63 ± 0.27) × 10^{-4}, closer to the value in CH$_4$. It can be noted that the C$_2$HD emission feature is weak and mixed with C$_2$H$_2$ emission features at the CIRS resolution (0.5 cm^{-1}). Coustenis et al. (2008) also detected a weak emission from the ν_4 band of C$_2$HD centered at 19.3 μm (519 cm^{-1}) in a large average of CIRS spectra (mixing disk and limb data). However, they did not analyze it due to the low S/N ratio and the presence of spurious instrumental features.

To overcome these difficulties and improve the precision in the D/H in acetylene, we used the Texas Echelon Cross Echelle Spectrograph (TEXES) on the NASA Infrared Telescope Facility (IRTF) to observe the ν_4 band of C$_2$HD at an unprecedented resolving power $\lambda/\Delta\lambda$ of ~65,000. We also observed spectral ranges around 8.0 and 13.4 μm to constrain the temperature profile and the C$_2$H$_2$ abundance profile in our radiative transfer analysis, in order to improve the accuracy of the C$_2$HD/C$_2$H$_2$ ratio determination.

2. TEXES observations

Observations of Titan were conducted with TEXES (Lacy et al., 2002) mounted at the NASA/IRTF on July 8 and 14, 2017 UT under programmes 2017A045 (PI: Bézard) and 2017A109 (PI: Nixon) respectively. We targeted three spectral intervals containing lines from C$_2$HD (518.4–520.0 cm^{-1}), C$_2$H$_2$ (742.9–746.7 cm^{-1}) and CH$_4$ (1244.3–1250.7 cm^{-1}). TEXES was used in the high-resolution cross-dispersed mode, achieving a resolving power between 65,000 and 95,000. Details of the observations are given in Table 1. Titan's angular size was 0.78 arcsec, less than the slit width (2.0 or 1.4 arcsec), so that our measurements pertain to disk-averaged conditions. The sub-Earth and sub-Sun latitudes were both 27°N. Observations occurred around Titan's summer solstice.

The C$_2$HD observations were performed by nodding Titan 5 arcsec along the 2.0 × 15 arcsec slit in order to remove the sky emission. For the C$_2$H$_2$ and CH$_4$ settings, the nodding amplitude was 3 arsec along the 1.4 × 9 and 1.4 × 7 arcsec slits respectively. The individual spectra were flat fielded, calibrated and co-added using the TEXES pipeline software package with the procedure described in Lacy et al. (2002). To remove the residual telluric absorption, we divided the Titan spectra by spectra of the asteroid 10 Hygiea recorded shortly after.

In a first step, we also relied on the 10 Hygiea spectra to obtain a flux calibration of our Titan observations. To do so, we used the asteroid Standard Thermal Model (STM) (Lebofsky and Spencer, 1989)

with the Earth distance, Sun distance and phase angle corresponding to our observations. We used the asteroid radius determined by Vernazza et al. (2021) (216.5 km) and the beaming parameter determined by Lim et al. (2005) (0.81). The Bond albedo and emissivity were taken as 0.07 and 0.98 respectively, as in Lim et al. (2005). The STM spectrum, calculated for zero solar phase angle, was corrected for phase by 0.01 magnitude per degree (10 Hygiea's phase angle was 3.5° for the July 8 observations and 5.8° for the July 14 observations). Titan's flux (in Jy) is then given by:

$$F_T = \frac{S_T}{S_a} F_a f, \tag{1}$$

where S_T and S_a are respectively the Titan and asteroid measured fluxes (in TEXES units), F_a is the asteroid flux (in Jy) and f a possible corrective factor (see Section 3), for now set to 1.

Fig. 1 shows the TEXES spectra in the three settings. In the C$_2$HD setting, we clearly detect several lines from the Q-branch of the C$_2$HD ν_4 band with a signal-to-noise (S/N) ratio up to 10. These lines appear on a continuum mostly due to N$_2$–CH$_4$ and N$_2$–H$_2$ collision-induced absorption and to haze emission. The C$_2$H$_2$ setting exhibits C$_2$H$_2$ lines of different intensities along with a H^{12}CN line, a weak H^{13}CN line and two weak emission features from C$_3$H$_8$. The CH$_4$ setting shows many strong and weak methane lines. The Titan-Earth Doppler shift of 15 km s^{-1} allowed us to observe the full low-frequency half of the Titan CH$_4$ strong lines. In all plots, regions of low telluric transmission have been removed.

3. Cassini/CIRS observations

Because the C$_2$HD, C$_2$H$_2$ and CH$_4$ lines were not recorded simultaneously in the TEXES spectra, the precision of the D/H ratio we are able to achieve is sensitive to any error in the relative flux calibration of the three settings. We expect that our flux calibration, based on the ratio between Titan and 10 Hygiea observations, is no more than 10%–15% accurate. Error sources come from possible flux variations of asteroid 10 Hygiea with rotational phase and possible spectral variations of its emissivity between the three TEXES settings. Also, variations in the atmospheric seeing and pointing errors can induce flux calibration errors.

To get around this difficulty, we employed spectra recorded by the Cassini Composite Infrared Spectrometer (CIRS; Flasar et al., 2004; Jennings et al., 2017) to calibrate our TEXES data. CIRS was a Fourier transform spectrometer, composed of three focal planes covering the spectral ranges 10–600 cm^{-1} (FP1), 580–1100 cm^{-1} (FP3) and 1050–1500 cm^{-1} (FP4) with a spectral resolution adjustable between 0.5 and 15 cm^{-1}. FP1 had a single detector with a circular field of view (FOV) of 3.9-mrad diameter while FP3 and FP4 each included a linear array of ten detectors providing an instantaneous field of view (IFOV) of 0.27 mrad (square). The CIRS absolute radiometric calibration is expected to be precise at the 1% level (Jennings et al., 2017) but great care must be taken in selecting the CIRS spectra for comparison with our disk-averaged TEXES observations.

Regarding the calibration of the C$_2$HD TEXES setting, we selected FP1 CIRS spectra recorded during a TEA (Titan Exploration at Apoapse) observational sequence designed to place Titan fully within the FP1 pixel (Nixon et al., 2019). Three TEA sequences are useable (CIRS_182TI_TEA001_PRIME, CIRS_202TI_TEA001_PRIME and CIRS_219TI_TEA001_PRIME). We chose to average the last two sequences in which the sub-spacecraft latitude is 0 and 51°N, the first
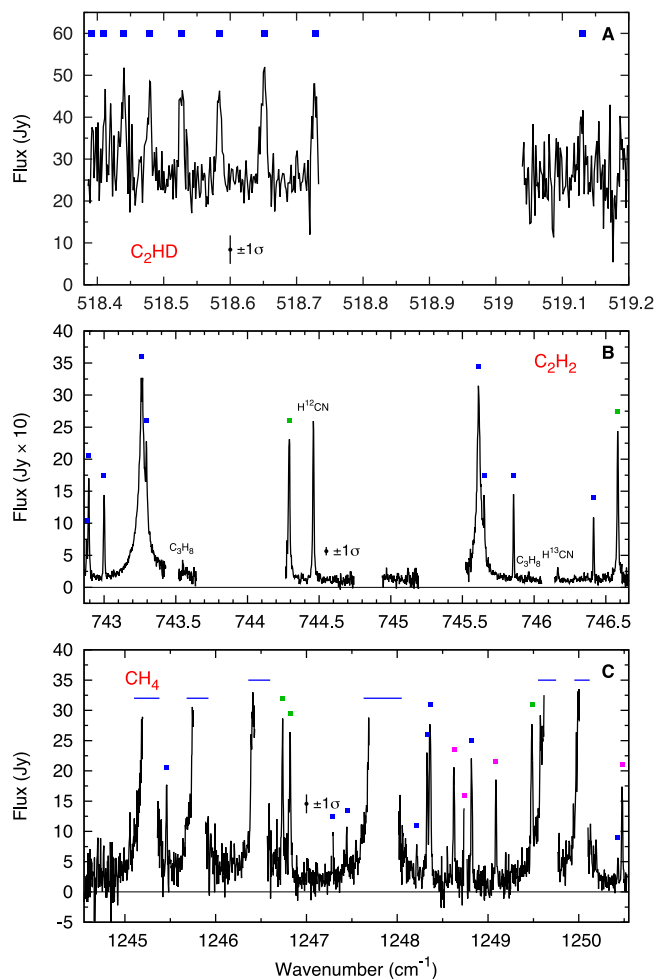
Fig. 1. TEXES spectra recorded in three spectral intervals containing lines of C$_2$HD (A), C$_2$H$_2$ (B) and CH$_4$ (C). Spectra have been flux-calibrated against 10 Hygiea observations using the asteroid STM (see text). In panel A, the locations of the C$_2$HD lines are indicated as blue squares. In panel B, all the detected lines are from C$_2$H$_2$, except for two HCN lines and two weak C$_3$H$_8$ features which are labeled. Blue squares indicate ^{12}C^{12}CH$_2$ lines and green squares ^{12}C^{13}CH$_2$ lines. In panel C, all lines are due to methane. Besides strong ^{12}CH$_4$ multiplets (horizontal blue lines), weaker lines from ^{12}CH$_4$ (blue squares), ^{13}CH$_4$ (green squares) and CH$_3$D (purple squares) are clearly detected. The $\pm 1\sigma$ noise error bars are indicated. Missing intervals in the data correspond to either troughs between grating orders or regions with low telluric transmission. (For interpretation of the references to color in this figure legend, the reader is referred to the web version of this article.)

one being 41°S, far from the 27°N of our TEXES observations. Details of the CIRS observations are given in Table 2. The resulting spectrum is shown in Fig. 2 along with a second-order polynomial fit over the range 460–560 cm^{-1} (a degree 2 for the polynomial fit is the one that minimizes the reduced χ^2). This fit indicates a continuum intensity of 0.396 ± 0.002 mW m^{-2} sr^{-1} / cm^{-1} at 519 cm^{-1} that we need to convert into a flux in Jy at the Titan-Earth distance of the TEXES observations (9.124 AU). However, this is not straightforward because the CIRS FP1 FOV is not homogeneous, being greatest at the center, reaching half power at 1.2 mrad from center and zero at 3.2 mrad (Flasar et al., 2004; Anderson and Samuelson, 2011). To do so, we used the FOV sensitivity function determined by Anderson and Samuelson (2011, Fig. 2) and a synthetic spectrum of Titan's emission calculated as a function of distance from disk center. This spectrum was generated from the radiative transfer and atmospheric models described in Section 4, with the haze opacity adjusted to reproduce the CIRS radiance at 519 cm^{-1}. Doing so, we expect a continuum flux

of 23.0 Jy in the TEXES observations around this wavenumber. This is about 6% lower than obtained by using the flux from the STM of 10 Hygiea, and we have then to set the corrective factor f in Eq. (1) to 0.94.

The CIRS FP3 and FP4 detectors have a much lower IFOV than FP1's FOV and there are no CIRS observing sequences in which Titan is fully included in their linear arrays. We then turned to the COMPMAP (Composition Map) sequences in which the FP3 and FP4 arrays were positioned to span Titan's disk in one to five positions (Nixon et al., 2019). We selected the one noted in Table 2 as it is closest in terms of time and in sub-solar and sub-instrument latitudes to the TEXES observations. We binned the observations into concentric rings of equal area, centered on Titan's disk and covering altogether 0 to 3050 km in radius (i.e up to 475 km above the surface). We then summed these bins and converted the result into a flux (Jy) at a Titan-Earth distance of 9.124 AU, as relevant for the July 8 TEXES observations. The FP3 and FP4 final spectra are shown in Fig. 3. We degraded the TEXES observations at the resolution of the CIRS spectra (0.53 cm^{-1}) with the help of a synthetic spectrum (see Section 4) to fill in the troughs in the TEXES data. From a least-squares fit approach, we then determined the corrective factor f in Eq. (1) to be 1.09 for the C$_2$H$_2$ setting and 0.86 for the CH$_4$ setting, taking into account the Titan-Earth distances of the observations (Table 1).

In the radiative transfer analysis of the TEXES observations, we used this CIRS-based flux calibration to which we assign an uncertainty of ±5%, arising from the construction of the CIRS disk averages and possible variations of the integrated disk flux. We note that the corrective factors we derived vary from 0.86 to 1.09, which seems reasonable given the uncertainty in the 10 Hygiea STM and possible pointing errors.

4. Radiative transfer analysis

Spectral modeling of the observations was performed with a line-by-line radiative transfer code coupled with an iterative inversion scheme (Conrath et al., 1998) as described in Vinatier et al. (2007a). Sources of molecular opacity are the collision-induced opacity (CIA) from N$_2$, CH$_4$ and H$_2$ pairs, ro-vibrational bands of CH$_4$, CH$_3$D, C$_2$H$_2$, C$_2$HD, HCN, C$_2$H$_6$ and C$_3$H$_8$, and absorption from aerosol particles. We used the CIA absorption coefficients from Borysow and Frommhold (1986), Karman et al. (2015) and Finenko et al. (2022). Line positions, energy levels and intensities of C$_2$H$_2$ and C$_2$HD come from GEISA2020 (Delahaye et al., 2021), the C$_2$HD parameters being based on the analysis of Jolly et al. (2008). For the N$_2$ pressure-broadened line widths and temperature exponents, we used the m-dependent values determined by Bouanich et al. (1998). Line parameters for the other molecules are the same as in Bézard et al. (2018). As regards the aerosol opacity, we used the spectral dependence recommended by Bézard and Vinatier (2020) (their Fig. 4), which is based on Vinatier et al. (2012) beyond 600 cm^{-1}. The integrated optical depth at the reference wavenumber of 1090 cm^{-1} is 0.029.

The atmospheric model includes vertical profiles of gas abundances, aerosol absorption and temperature. The CH$_4$ profile is fixed to that derived by Niemann et al. (2010) from Huygens in situ measurements. For the other molecular species and the aerosol opacity, we adopted the profiles retrieved by Vinatier et al. (2020) from Cassini/CIRS limb and nadir measurements recorded on September 11, 2017 at 21°N. Note that the corresponding C$_2$H$_2$ profile is only used as an a priori (first guess) profile in the retrievals of the C$_2$H$_2$ profile from TEXES measurements. This is also true for the HCN profile. All other absorber abundance profiles are left unchanged in the retrieval code.

The temperature profile that serves as an a priori profile in the inversion process is the 21°N profile (September 11, 2017) from Vinatier et al. (2020) down to the 10-mbar level. In the troposphere, the profile is constrained to reproduce two selections of FP1 spectra (15-cm^{-1} resolution) from 55 to 545 cm^{-1}, recorded in 2016–2017 between 0°
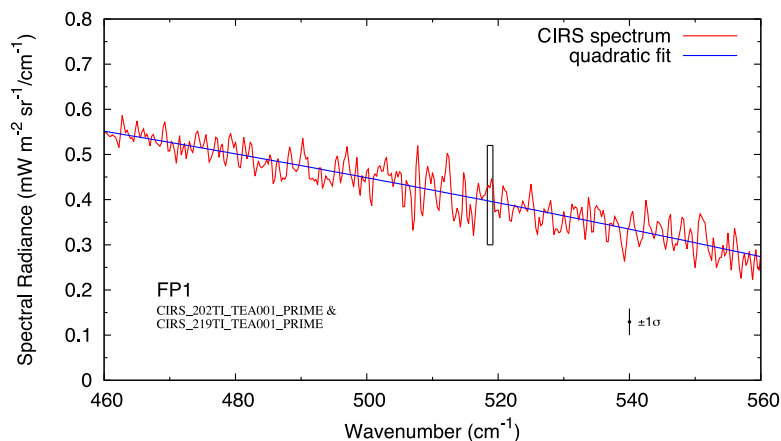
Fig. 2. FP1 Cassini/CIRS spectral average along with a second-order polynomial least-squares fit. The FP1 circular FOV encompasses the whole Titan disk. The narrow rectangle around 519 cm^{-1} indicates the location and width of the C$_2$HD TEXES interval. The $\pm 1\sigma$ noise error bars are indicated.

Table 2
Cassini/CIRS observations of Titan (resolution = 0.5 cm^{-1}).

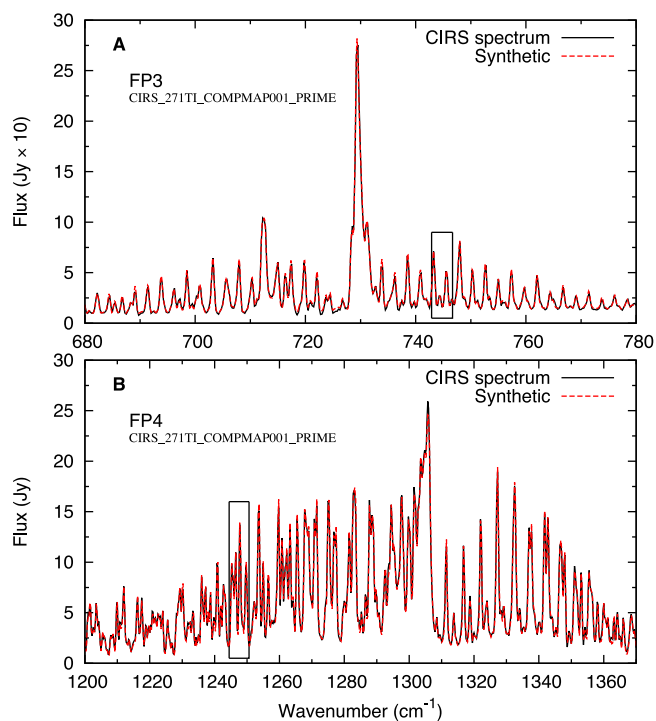| Sequence	Focal plane	Date	Distance (km)	Number of spectra	Sub-solar latitude	Sub-spacecraft latitude
CIRS_202TI_TEA001_PRIME	FP1	March 02–03, 2014	1,522,600	891	21°N	51°N
CIRS_219TI_TEA001_PRIME	FP1	July 23–24, 2015	1,580,500	784	25°N	0°
CIRS_271TI_COMPMAP001_PRIME	FP3, FP4	April 23–24, 2017	761,800 – 917,000	3613 (FP3) 3606 (FP4)	27°N	17°N

Fig. 3. FP3 (Panel A) and FP4 (Panel B) Cassini/CIRS spectral averages along with best fit models. Fluxes correspond to a Titan–Earth distance of 9.124 AU. The rectangles around 745 cm^{-1} and 1248 cm^{-1} indicate the location and width of the C$_2$H$_2$ and CH$_4$ TEXES intervals respectively. The noise equivalent spectral flux is 0.6 Jy in Panel A (∼0.7 times the line thickness) and 0.10 Jy in Panel B (similar to the line thickness).

and 40°N and from a distance of $(7.5–9.5) \times 10^4$ km from Titan. The first one is characterized by a "low" mean emission angle of 13.1° and the second one a "high" mean emission angle of 54.2°.

Spectra are calculated using an atmospheric grid of 70 layers equally spaced in log p from the surface up to $p = 0.15$ µbar (∼600 km). For Cassini/CIRS modeling, monochromatic spectra are convolved with a Hamming function of resolution 0.528 cm^{-1} (distance of first zero). For TEXES modeling, the convolution function is a Gaussian with the full width at half-maximum given in Table 1. Radiance spectra are calculated for five lines-of-sight intercepting the surface from disk center to the solid radius and for six lines-of-sight above the surface at altitudes up to 475 km. These two regions are divided into respectively five and six circular rings of equal area. The distance of the lines of sight to disk center is taken as the average of the radii of the concentric circles delimiting each annulus. The intensities are then summed with weights equal to the circular ring areas to produce an integrated flux spectrum.

The inversion algorithm minimizes a weighted sum of the residuals between synthetic and observed spectrum (i.e. the χ^2) and between solution and a priori profile (temperature or mole fraction) (see details in Vinatier et al., 2007a). A correlation length (L) of one pressure scale height is further used for filtering the solution profile. The disk-averaged temperature profile in the stratosphere was retrieved from the methane emission spectrum in the 1200–1370 cm^{-1} range for the CIRS measurements and 1244.7–1250.5 cm^{-1} for the TEXES measurements, assuming that the stratospheric methane mole fraction is constant with altitude and over the disk (1.48%; Niemann et al., 2010). In fact, by simultaneously analyzing FP1 and FP4 Cassini/CIRS spectra at different latitudes, Lellouch et al. (2014) showed that the stratospheric methane abundance varies within a range of 1 to 1.5% as a function of latitude. In particular, the ∼1% mole fraction derived at low latitudes agrees with the reanalysis of the Huygens Descent Imager/Spectral Radiometer (DISR) data by Rey et al. (2018). The CH$_4$ abundance profile they derived is lower than the Huygens/GCMS profile (Niemann et al., 2010) above ∼39 km and reaches ∼1% above 110 km. Consequently, we also

ran an alternative case in which we used the Rey et al. (2018) methane profile in place of the Niemann et al. (2010) profile (see Section 5).

The disk-averaged acetylene profile was retrieved from the 679–780 cm^{-1} interval for the CIRS measurements and 742.8–746.6 cm^{-1} for the TEXES measurements. The C_2HD/C_2H_2 ratio (assumed to be constant with altitude) was inferred from the TEXES measurements combining the intervals 518.38–518.73 and 519.08–519.17 cm^{-1}. The aerosol optical depth at the reference wavenumber was simultaneously retrieved.

The procedure we followed in this analysis is the following:

(a) retrieve the temperature profile from the disk-averaged CIRS FP4 selection using the Vinatier et al. (2020) 21°N profile as a first guess $\longrightarrow T_{CIRS}(p)$

(b) retrieve the temperature profile from the TEXES measurements (CH_4 setting and continuum in the C_2HD setting) taking $T_{CIRS}(p)$ as the a priori profile $\longrightarrow T_{TEXES}(p)$

(c) retrieve the C_2H_2 profile from the disk-averaged CIRS FP3 selection with the Vinatier et al. (2020) 21°N profile for a priori profile and $T_{CIRS}(p)$ for the temperature profile $\longrightarrow q_{CIRS}(p)$

(d) retrieve the C_2H_2 profile from the TEXES measurements (C_2H_2 setting) using $q_{CIRS}(p)$ for the a priori profile and $T_{TEXES}(p)$ for the temperature profile $\longrightarrow q_{TEXES}(p)$

(e) determine the C_2HD/C_2H_2 ratio from the TEXES measurements (C_2HD setting) using $T_{TEXES}(p)$ for the temperature profile and $q_{TEXES}(p)$ for the C_2H_2 profile

We also performed some tests in which we used the Huygens/HASI temperature profile (Fulchignoni et al., 2005) recorded in situ at 10°S as the a priori profile in Step a or directly in Step b. As regards Step e, we tested an additional case in which we use the CIRS-derived temperature ($T_{CIRS}(p)$) and acetylene ($q_{CIRS}(p)$) profiles to derive the C_2HD/C_2H_2 ratio (see next section).

5. Results

The temperature profile retrieved from the inversion of the CIRS FP4 average ($T_{CIRS}(p)$) is shown in Fig. 5 and the corresponding model fit to the data is shown in Fig. 3b. The observations are sensitive to the 0.03–11 mbar range (95–350 km) (Fig. 6). In the 0.1-mbar region, this profile is warmer than the a priori profile, which refers to latitudes around 21°N, while the situation is reversed in the 1–10 mbar range. This is expected as the CIRS spectral average incorporates latitudes that are on the average warmer than mid-northern latitudes around 0.1 mbar and cooler in the 1–10 mbar pressure range, as can be seen in Fig. 2 of Vinatier et al. (2020).

In a second step, this CIRS-inverted profile was used as an a priori profile to retrieve a temperature profile $T_{TEXES}(p)$ from the TEXES observations around 1248 cm^{-1}. This profile is shown in Fig. 5 and the corresponding fit of the data in Fig. 4a. The higher spectral resolution of the TEXES data allows us to somewhat tighten the constraints in the lower stratosphere down to about 15 mbar (85 km) (Fig. 6). In the inversion procedure, we also used data in small spectral intervals in the continuum around 518.5–518.7 cm^{-1} to constrain the (near-)surface temperature. The CIRS– and TEXES–retrieved temperature profiles are very similar and differ by at most 1.5 K in the 2–mbar region.

A C_2H_2 profile $q_{CIRS}(p)$ was first obtained from the CIRS FP3 spectral average using the 21°N profile of Vinatier et al. (2020) as the a priori in the inversion process (Fig. 5). The fit to the data is shown in Fig. 3a. The region probed ranges from 0.12 mbar (275 km) to 18 mbar (80 km) (Fig. 6). The TEXES data around 745 cm^{-1} were then used to retrieve the final C_2H_2 profile ($q_{TEXES}(p)$) shown in blue in Fig. 5 using the CIRS-retrieved profile as the a priori. The fit of the data and the residuals are shown in Fig. 4b. As for temperature, the high resolution of the TEXES observations allows us to slightly improve the constraints on the disk-averaged C_2H_2 profile, extending the region probed to ∼0.10–20 mbar (75–285 km). The TEXES-derived C_2H_2 mole fraction is some
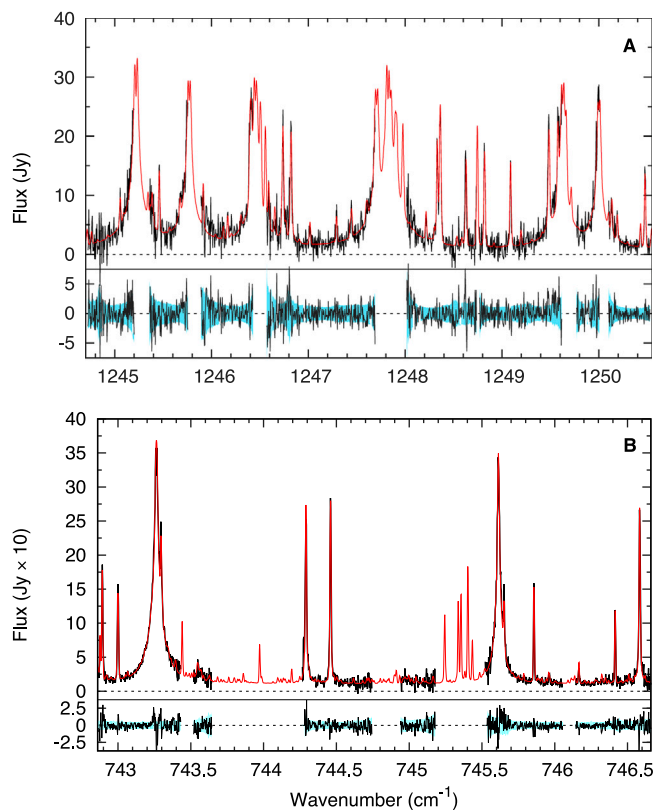

Fig. 4. Best model fit (red) to observed TEXES (black) spectrum in the CH_4 setting around 1248 cm^{-1} (Panel A) and in the C_2H_2 setting around 745 cm^{-1} (Panel B). The lower sub-panels in both panels show the residuals of the fit (black) along with the $\pm 1\sigma$ noise envelope (cyan). The TEXES spectra are calibrated against Cassini/CIRS spectral averages (see Section 3). (For interpretation of the references to color in this figure legend, the reader is referred to the web version of this article.)

35% smaller than the CIRS-derived one in the 0.2–0.5 mbar range and about 20% larger from 4 to 15 mbar.

The formal 1–SD noise errors on the TEXES-retrieved profiles are 0.2 K in the 0.03–15 mbar range for the temperature and 2% for the C_2H_2 mole fraction in the 0.10–20 mbar. We evaluated the model errors from the variations induced in the retrieved profiles by a change in the a priori temperature and C_2H_2 abundance profiles used in Steps (a) and (c). To do so, we considered a priori profiles that differ from the Vinatier et al. (2020) 21°N profiles above the 20-mbar level by ± 10 K (temperature) and factors of 0.5 or 2 (C_2H_2). The so-derived error bars are shown in Fig. 5 at a few pressure levels.

Finally, we used the TEXES C_2HD setting around 519 cm^{-1} to retrieve the C_2HD/C_2H_2 ratio using the TEXES-derived temperature profile $T_{TEXES}(p)$ and C_2H_2 profile $q_{TEXES}(p)$. In the inversion process, the C_2HD/C_2H_2 ratio is assumed to be constant with altitude and we thus solved for only one parameter (technically this is done by fixing a very large value for the correlation length L, 100 times the pressure scale height). We derived a C_2HD/C_2H_2 ratio that corresponds to a D/H ratio of $(1.14 \pm 0.04) \times 10^{-4}$, where the error bars account only for the noise equivalent flux in the TEXES C_2HD observations and correspond to a χ^2 variation of 1. The model fit to the observations is shown in Fig. 7. Our measurement is most sensitive to the region between 0.7 and 16 mbar (Full Width at Half Maximum of the contribution function), with the contribution function peaking at 6 mbar (115 km) (Fig. 6).

We investigated different sources of error. We made a first test in which we used the CIRS-derived atmospheric model ($T_{CIRS}(p)$ and $q_{CIRS}(p)$) to model the C_2HD TEXES lines. We then derived a D/H ratio of $(1.09 \pm 0.04) \times 10^{-4}$, i.e. 5% smaller than when the temperature and acetylene profiles are derived from the CH_4 and C_2H_2 TEXES settings.
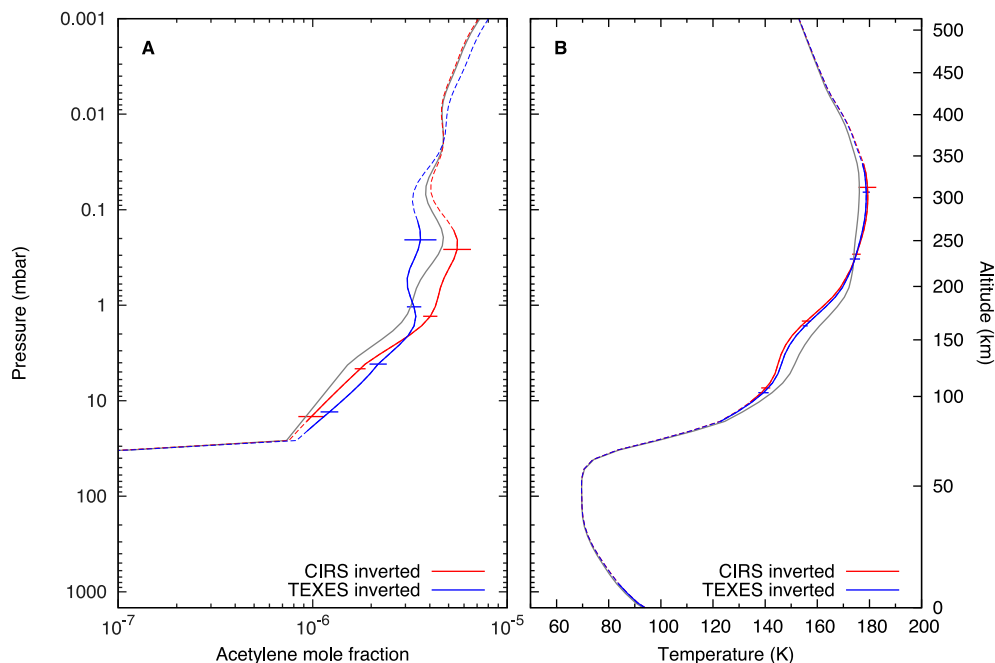
Fig. 5. Vertical profiles of C_2H_2 (Panel A) and temperature (Panel B) retrieved from the Cassini/CIRS (red) and TEXES (blue) data. A stratospheric methane abundance of 1.48% was used in the temperature retrievals. The gray profiles are the a priori (Vinatier et al., 2020) profiles used in the inversion of the CIRS spectral averages. The solid colored lines correspond to the regions to which the data are sensitive. The formal 1–SD noise errors on the TEXES-retrieved profiles and the regions probed by the observations are: 0.2 K (0.03–15 mbar) for the temperature and 2% for the C_2H_2 mole fraction (0.10–20 mbar). The total error bars, including those from model uncertainties, are indicated at a few selected levels. (For interpretation of the references to color in this figure legend, the reader is referred to the web version of this article.)
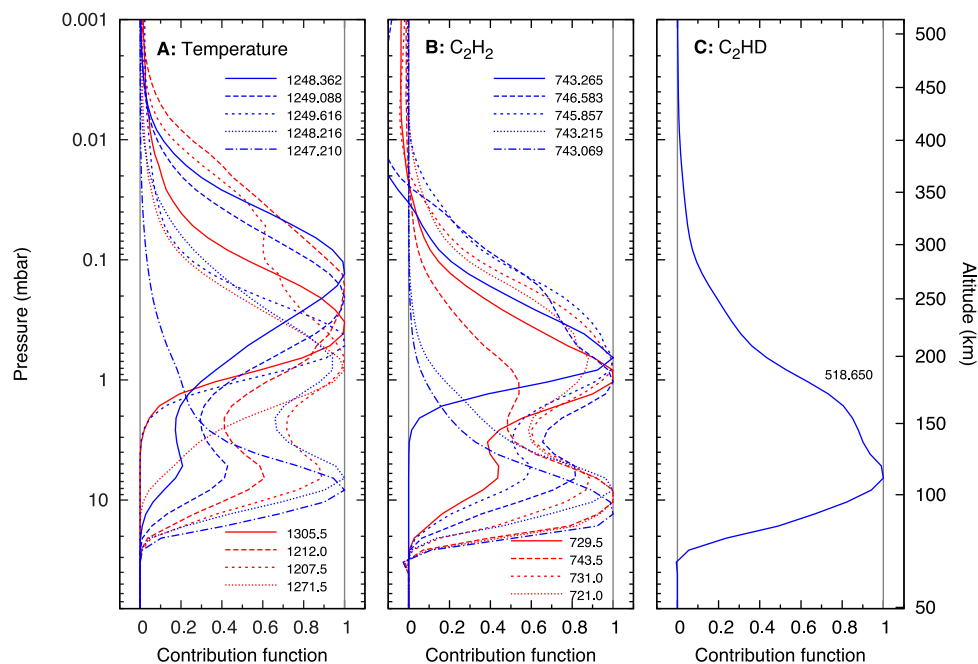

Fig. 6. Contribution functions at selected wavenumbers calculated for the best-fitting models (Fig. 5) of CIRS (red lines) and TEXES (blue lines) observations. These contribution functions, which have been normalized at each wavenumber, are Jacobians that give the rate of change of spectral flux with temperature (Panel A), logarithm of C_2H_2 mole fraction (Panel B), and logarithm of C_2HD mole fraction (Panel C). (For interpretation of the references to color in this figure legend, the reader is referred to the web version of this article.)

We also tested the sensitivity of the derived D/H ratio to assumptions about the a priori profiles used in the retrieval process. First we used the Huygens/HASI profile (Fulchignoni et al., 2005) as the a priori profile for the temperature retrievals from Cassini/CIRS data (Step a) or directly for the temperature retrievals from TEXES data (Step b). In either case, the so-derived D/H ratio is within 1% of our nominal value. Secondly, we considered the propagation of the model errors

mentioned above into the retrieved D/H ratio. A variation of the a priori temperature model by ±10 K induces a change by ±3% in the derived D/H ratio while a variation of the a priori acetylene model by a factor of two causes negligible variations of the retrieved D/H ratio (<1%).

As discussed in Section 4, we also ran a case in which the temperature was retrieved using the Rey et al. (2018) methane profile,
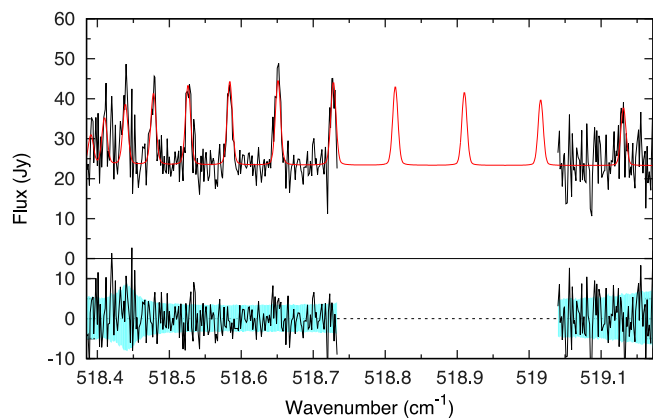
Fig. 7. Best model fit (red) to observed TEXES (black) spectrum in the C_2HD setting around 519 cm^{-1}. The lower sub-panel shows the residuals of the fit (black) along with the $\pm 1\sigma$ noise envelope (cyan). The TEXES spectrum is calibrated against a Cassini/CIRS spectral average (see Section 3). (For interpretation of the references to color in this figure legend, the reader is referred to the web version of this article.)

Table 3
Relative uncertainties on the derived D/H ratio in acetylene.

Origin	Relative error
Noise (1σ)	$\pm 3.5\%$
Use CIRS T and q	-5%
T and q model errors	$\pm 3\%$
CH_4 abundance	$+8\%/-7\%$
5% flux error in:	
– C_2HD setting	$\pm 6\%$
– C_2H_2 setting	$+17\%/-12\%$
– CH_4 setting	$\pm 5.5\%$
Band intensity	$\pm 4\%$
Total	$+22\%/-17\%$

which has a stratospheric CH_4 abundance of 1% instead of the 1.48% mole fraction from Niemann et al. (2010). In this case, the derived temperature profile is warmer by at most 2.6 K at 1.3 mbar and by 1.2 K at 0.25 and 10 mbar. The derived C_2H_2 mole fraction is consequently lower by up to -32% around 1 mbar while the D/H ratio reaches 1.31×10^{-4}, the C_2HD lines being less sensitive to temperature change than the optically thick C_2H_2 lines. Because the methane mole fraction varies over Titan's disk between 1 and 1.5% (Lellouch et al., 2014), we retained for the nominal value of the D/H ratio the (geometrical) mean of the values retrieved for the Niemann et al. (2010) and for the Rey et al. (2018) CH_4 profiles, these values providing the conservative upper and lower limits: D/H (in C_2H_2) = $(1.22^{+0.09}_{-0.08}) \times 10^{-4}$.

We also considered a 5% flux calibration error in each of the three TEXES settings and finally took into account the $\pm 4\%$ uncertainty of the C_2HD band intensity reported by Jolly et al. (2008). The errors induced on the D/H ratio are listed in Table 3. Combining quadratically these different error sources, we obtain a relative error of $+22\%/-17\%$, leading to:

D/H (in C_2H_2) = $(1.22^{+0.27}_{-0.21}) \times 10^{-4}$

We note that an important source of error is that due to the flux calibration of the C_2H_2 setting. A 5% variation of the flux scale causes a change of the retrieved C_2H_2 abundance profile of 24% at 1 mbar, 11% at 5 mbar and 6% at 10 mbar. The induced change on the C_2HD/C_2H_2 ratio is then $+17\%/-12\%$. The second most significant source of error is the uncertainty on the disk-averaged stratospheric CH_4 used in the temperature retrievals.

6. Discussion

The value we retrieved for the D/H ratio in acetylene $(1.22^{+0.27}_{-0.21} \times 10^{-4})$ is significantly smaller than that derived by Coustenis et al.

(2008) from different selections of Cassini/CIRS nadir spectra over Titan's disk ($2.09 \pm 0.45 \times 10^{-4}$). It is also marginally smaller than the value derived by the same authors from Cassini/CIRS limb data at four different latitudes, averaging to $1.63 \pm 0.27 \times 10^{-4}$, although their error bars clearly overlap with ours. These CIRS determinations are made difficult by the weakness of the C_2HD emission in the 678-cm^{-1} ν_5 band at the instrument's resolution of 0.5 cm^{-1}. In addition, the part of the analysis limited to surface-intercepting measurements suffers from the lack of a precise determination of the C_2H_2 vertical profile from the data, which has a strong influence on the retrieved C_2HD/C_2H_2 ratio. On the other hand, the precision of our measurement is mostly limited by the fact that we do not observe the C_2HD and C_2H_2 lines simultaneously. We have then to rely on a relative calibration of the two instrumental settings for which we used Cassini/CIRS spectral averages as representative as possible of the observing conditions of TEXES (period, sub-solar and sub-instrument latitudes).

The D/H ratio in acetylene we obtained is consistent, within error bars, with the D/H ratio measured in methane from Cassini/CIRS measurements by Bézard et al. (2007) ($1.32^{+0.15}_{-0.11} \times 10^{-4}$), Coustenis et al. (2007) ($1.17^{+0.23}_{-0.28} \times 10^{-4}$), Abbas et al. (2010) ($1.58 \pm 0.16 \times 10^{-4}$) and Nixon et al. (2012) ($1.59 \pm 0.27 \times 10^{-4}$) and from the ground-based measurements by Penteado et al. (2005) ($1.25 \pm 0.25 \times 10^{-4}$) and de Bergh et al. (2012) ($1.13 \pm 0.25 \times 10^{-4}$), indicating altogether a value in the range $(1.1–1.6) \times 10^{-4}$.

This result suggests no significant fractionation of deuterium in acetylene compared with methane, the main atmospheric reservoir of hydrogen. On the other hand, as first investigated by Pinto et al. (1986) and then Lunine et al. (1999), a source of fractionation in the methane photochemistry lies in the higher energy of the C–D bond compared with the C–H bond. These authors considered that methane is most efficiently destroyed by the abstraction reactions:

$$C_2H + CH_4 \rightarrow C_2H_2 + CH_3 \quad \quad (k_1)$$

$$C_2H + CH_3D \rightarrow C_2H_2 + CH_2D \quad \quad (k_{2a})$$

$$\rightarrow C_2HD + CH_3 \quad \quad (k_{2b})$$

From consideration of chemical kinetics of some deuterated species, Lunine et al. (1999) argued that q, equal to $(k_{2a} + k_{2b})/k_1$, lies in the range 0.80–0.88. Because the ratio of the reaction coefficients q is lower than 1, CH_4 destruction is favored over CH_3D destruction, opening up the possibility of a deuterium fractionation in the photochemical products. We define q' as the ratio of the intrinsic probability of breaking a C–D bond to that of breaking a C–H bond, or equivalently by the ratio $3k_{2b}/k_{2a}$. If we further assume that k_{2a} is equal to 0.75 k_1, given that Reaction 2a does not break the C–D bond, then $q' = 3k_{2b}/k_{2a} = 4k_{2b}/k_1$ is in the range 0.2–0.52.

According to the photochemical model of Vuitton et al. (2019), photolysis of ethylene (C_2H_4) is the main source of acetylene in the bulk of the atmosphere. This production peaks around 300 km. Ethylene is mostly produced in the upper atmosphere (~800 km) from the reaction of the CH radical with methane and flows down to the stratosphere where it is mostly lost by photolysis. In Appendix, we use a simplified 0-D photochemical model to identify possible fractionation processes in the production of C_2H_2 linked to the expected higher binding energy of the C–D bond. We found that fractionation of deuterium can occur at two stages: in the formation of the CH radical from the $^3CH_2$ radical and from the photolysis of C_2H_4. Both of them tend to enhance the D/H ratio in C_2H_4 and thus in C_2H_2. If the q' ratios associated to these two reactions were similar to that for $C_2H + CH_4$ mentioned above (0.2–0.52), the D/H in C_2H_2 would be as high as 1.4–1.9 times that in CH_4 (Eq. (5)), which is not what we observe. On the other hand, if fractionation were limited to the CH radical formation stage (i.e., assuming no fractionation through the C_2H_4 photolysis), the fractionation factor would be lower (1.08–1.17) and compatible with the

D/H measurement errors. This implies that either the kinetic isotope effect (KIE) in the photodissociation of C_2H_4 is not as strong as in the $C_2H + CH_4$ reaction considered by Lunine et al. (1999), or that other photochemical processes that we did not consider in Appendix mitigate this KIE.

7. Conclusions

We report here the first observation of several lines from the Q-branch of the ν_4 band of C_2HD on Titan at 19.3 μm. Combining observations of C_2HD, C_2H_2 and CH_4 lines with the same instrument (IRTF/TEXES) and using Cassini measurements for the flux calibration, we derived a value for the D/H ratio in acetylene of $(1.22^{+0.27}_{-0.21}) \times 10^{-4}$. This value is consistent within error bars with the D/H ratio measured in methane. Our main source of uncertainty arises from the relative flux calibration of the three different settings we used to record the C_2HD, C_2H_2 and CH_4 lines. Improving on the flux calibration, e.g. by observing these emissions simultaneously, would allow us to reduce significantly the error bars on the D/H ratio in acetylene. Recent observations by the MIRI medium-resolution spectrometer (MRS) aboard the James Webb Space Telescope (JWST) conducted in July 2023 (Titan project GTO 1251) may help in this regard once issues in fringe removal and flux calibration have been resolved.

While our result indicates no significant deuterium fractionation in acetylene relative to methane, at least in the region probed (0.7–16 mbar; 80–190 km), we have identified two possible processes in the photochemical production of C_2H_2 that should in theory enhance the D/H ratio in acetylene. These are the formation of the CH radical from the $^3CH_2$ radical and the photodissociation of C_2H_4. This potential enhancement arises from the fact that the C–D bond is slightly stronger than the C–H bond. Laboratory measurements of the KIEs for these two reactions, most importantly for the C_2H_4 photolysis, would be very valuable. It would be also useful that complete photochemical models incorporate deuterium species, even with approximative KIEs, to investigate the deuterium fractionation in various hydrocarbons. From an observational standpoint, signatures from other deuterated hydrocarbons (e.g. C_2H_6, C_2H_4) could also be sought in Titan's spectrum to better constrain its atmospheric photochemistry.

CRediT authorship contribution statement

B. Bézard: Writing – original draft, Supervision, Investigation, Formal analysis, Conceptualization. **C.A. Nixon:** Writing – review & editing, Data curation. **S. Vinatier:** Writing – review & editing, Validation, Conceptualization. **E. Lellouch:** Writing – review & editing, Validation, Conceptualization. **T. Greathouse:** Writing – review & editing, Data curation. **R. Giles:** Writing – review & editing, Data curation. **N.A. Lombardo:** Writing – review & editing, Conceptualization. **A. Jolly:** Investigation, Formal analysis, Conceptualization.

Declaration of competing interest

The authors declare that they have no known competing financial interests or personal relationships that could have appeared to influence the work reported in this paper.

Data availability

The raw TEXES data used in this study can be obtained from the NASA/IRTF archive at https://irsa.ipac.caltech.edu/applications/irtf/. The product IDs for the three spectral settings (C_2HD, C_2H_2 and CH_4) are:

Titan C_2HD: TX17A0708.1038-1045
10 Hygiea C_2HD: TX17A0708.1035-1036
Titan C_2H_2: TX17A0714.6004-6017

10 Hygiea C_2H_2: TX17A0714.6018-6019
Titan CH_4: TX17A0708.1030-1033
10 Hygiea CH_4: TX17A0708.1017-1028

The raw data were calibrated using the 2017 version of the TEXES pipeline software (current version is available at https://github.com/TEXESArch/pipecode). The reduced data presented in this study are archived (Bézard et al., 2024) as ascii files at https://data.mendeley.com/datasets/pb6f6rrypb/1.

Appendix. Fractionation in the production of C_2H_2

Potential sources of isotopic fractionation in the photochemistry of methane include photochemical reactions (molecular, ion-molecule and photodissociation), atmospheric escape, condensation/evaporation and molecular diffusion. We investigate here how the photochemical production of C_2H_2 from methane photochemistry could lead to a deuterium fractionation due to the greater strength of the C–D bond compared to the C–H bond. To do so, we only considered the major chemical steps leading to the formation and loss of C_2H_2 (through 0-D calculations), based on the photochemical model of Vuitton et al. (2019). We further assumed that a reaction of a species A (radical or molecule) with a deuterated hydrocarbon B has the same reaction rate k as with the main isotopologue if it does not break the C–D bond and a rate $q'k$, with $0 \leq q' \leq 1$, if the C–D bond is broken. The same is assumed for a photodissociation reaction.
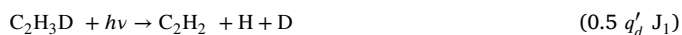
According to Vuitton et al.'s (2019) model, C_2H_2 is mostly formed by photodissociation of C_2H_4 in the upper stratosphere ($\sim$300 km):

$$C_2H_4 + h\nu \rightarrow C_2H_2 + 2H \tag{J_1}$$

$$\rightarrow C_2H_2 + H_2, \tag{J_2}$$

and accordingly for C_2HD by:

$$C_2H_3D + h\nu \rightarrow C_2HD + 2H \tag{0.5 J_1}$$

$$\rightarrow C_2HD + H_2 \tag{0.5 J_2}$$

Note that in addition, C_2H_3D can be dissociated as:

$$C_2H_3D + h\nu \rightarrow C_2H_2 + H + D \tag{0.5 q'_d J_1}$$

$$\rightarrow C_2HD + HD \tag{0.5 q'_d J_2}$$

C_2H_2 and C_2HD are both lost by vertical transport to the condensation region in the lower stratosphere ($\sim$70 km), with a loss rate proportional to the species number density in this formation region: $K_1 [C_2H_2]$ and $K_1 [C_2HD]$. We neglect here the small vapor pressure isotope effect in the relative condensation loss of the two isotopologues. Equaling the production and loss rates for both isotopologues yields: $[C_2H_2] = J_1 [C_2H_4]/K_1$ and $[C_2HD] = 0.5 J_1 [C_2H_3D]/K_1$, so that

$$[D/H]_{C_2H_2} = 0.5 [C_2HD]/[C_2H_2] = 0.25 [C_2H_3D]/[C_2H_4] = [D/H]^1_{C_2H_4}, \tag{2}$$

where the latter term is the D/H ratio in ethylene in the formation region of acetylene (upper stratosphere).

Ethylene is transported from its formation region in the thermosphere where it has a D/H ratio that we denote $[D/H]^0_{C_2H_4}$. The C_2H_4 used to produce C_2H_2 is therefore supplied by a source having this D/H ratio and lost by photolysis with a C_2H_3D to C_2H_4 loss ratio equal to $0.5\ (1 + q'_d)\ J\ [C_2H_3D]/(J\ [C_2H_4]) = 0.5\ (1 + q'_d)\ [C_2H_3D]/[C_2H_4]$, with $J = J_1 + J_2$. Therefore, in steady state and neglecting other sinks for ethylene, we obtain:

$$[D/H]^1_{C_2H_4} = 2/(1 + q'_d)\,[D/H]^0_{C_2H_4} \tag{3}$$

Photodissociation of ethylene thus appears as a potential source of enhancement of the D/H ratio in this species and consequently in acetylene, provided that $q'_d < 1$.
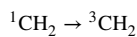
Following Vuitton et al. (2019), we assume that the bulk of ethylene is formed in the thermosphere, around 800 km, through the reaction:

$$CH + CH_4 \rightarrow C_2H_4 + H, \tag{k_1}$$
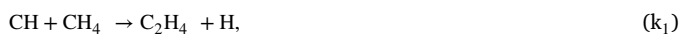
while C_2H_3D is accordingly formed by:

$$CH + CH_3D \rightarrow C_2H_3D + H, \text{ and} \tag{0.75 k_1}$$

$$CD + CH_4 \rightarrow C_2H_3D + H \tag{k_1}$$

The CH radical is mostly formed from the suite of reactions:

$$CH_4 + h\nu \rightarrow {}^1CH_2 + 2H \tag{J_3}$$

$${}^1CH_2 \rightarrow {}^3CH_2$$

$${}^3CH_2 + H \rightarrow CH + H_2, \tag{k_2}$$

where ${}^3CH_2$ is the methylene radical in the ground electronic state X^3B_1 and ${}^1CH_2$ the methylene radical in the excited state a^1A_1. The CHD radical is formed through:

$$CH_3D + h\nu \rightarrow {}^1CHD + 2H \tag{0.5 J_3}$$

and lost through:

$${}^3CHD + H \rightarrow CD + H_2 \tag{0.5 k_2}$$

$$\rightarrow CH + HD \tag{0.5 q'_f k_2}$$

The former reaction also forms CD, which is lost through the $CD + CH_4$ reaction mentioned above.

Balancing production and loss rates for each radical and assuming $[CH_3D] \ll [CH_4]$ yields:

$$[{}^3CH_2] = J_3[CH_4]/(k_2[H]),$$

$$[CH] = J_3/k_1,$$

$$[{}^3CHD] = J_3[CH_3D]/(k_2(1 + q'_f)[H]), \text{ and}$$

$$[CD] = (0.5/(1 + q'_f))J_3[CH_3D]/(k_1[CH_4]).$$

Ethylene is mostly lost by downward transport, a process that is not isotope-selective and proportional to the number density. Denoting the loss rates for the two isotopologues as $K_0\ [C_2H_4]$ and $K_0\ [C_2H_3D]$ and again balancing production and loss rates, we obtain:

$$[C_2H_4] = J_3[CH_4]/K_0,$$

$$[C_2H_3D] = J_3[CH_3D](0.75 + 0.5/(1 + q'_f))/K_0$$

The D/H ratio in ethylene in its production region is then given by:

$$[D/H]^0_{C_2H_4} = (0.75 + 0.5/(1 + q'_f))\,[D/H]_{CH_4} \tag{4}$$

A fractionation of deuterium may then occur in the production of ethylene, linked to the reaction of the methylene radical (CH_2) with the H atom. Combining Eqs. (2)–(4), the D/H ratio in acetylene in this simplified model is equal to:

$$[D/H]_{C_2H_2} = 2(0.75 + 0.5/(1 + q'_f))/(1 + q'_d)\,[D/H]_{CH_4} \tag{5}$$

If the q' factors associated to C_2H_4 photodissociation (q'_d) and to reaction of CH_2 with H (q'_f) were in the range of that for the $C_2H + CH_4$ reaction ($q' = 0.2$–0.52 according to Lunine et al., 1999), the D/H ratio in acetylene would be enhanced by a factor in the range 1.42–1.94 compared to the ratio in methane. This is not consistent with our measurement. On the other hand, if fractionation were only effective for the $CH_2 + H$ reaction and not for the C_2H_4 photodissociation ($q'_d = 1$), the fractionation factor would amount to 1.08–1.17, which is compatible with our result, given the errors associated with D/H ratio measurements in acetylene and methane. The kinetic isotope effect (KIE) in C_2H_4 photodissociation appears to be potentially the most important factor in the deuterium fractionation in acetylene. Our result of D/H in C_2H_2 being so similar to that in CH_4 suggests that the D/H fractionation in C_2H_2 via the photolysis of C_2H_4 should be weaker than in the catalytic destruction of methane through the $C_2H + CH_4$ reaction.

References

Abbas, M.M., Kandadi, H., LeClair, A., Achterberg, R.K., Flasar, F.M., Kunde, V.G., Conrath, B.J., Bjoraker, G., Brasunas, J., Carlson, R., Jennings, D.E., Segura, M., 2010. D/H ratio of Titan from observations of the Cassini/composite infrared spectrometer. Astrophys. J. 708 (1), 342–353. http://dx.doi.org/10.1088/0004-637X/708/1/342.

Anderson, C.M., Samuelson, R.E., 2011. Titan's aerosol and stratospheric ice opacities between 18 and 500 μm: Vertical and spectral characteristics from Cassini CIRS. Icarus 212 (2), 762–778. http://dx.doi.org/10.1016/j.icarus.2011.01.024.

Bézard, B., Greathouse, T.K., Giles, R., 2024. The D/H ratio in Titan's acetylene from high spectral resolution IRTF/TEXES observations: TEXES spectra of Titan and 10 Hygiea. Mendeley data, v1. http://dx.doi.org/10.17632/pb6f6rrypb.1.

Bézard, B., Nixon, C.A., Kleiner, I., Jennings, D.E., 2007. Detection of ^{13}CH$_3$D on Titan. Icarus 191 (1), 397–400. http://dx.doi.org/10.1016/j.icarus.2007.06.004.

Bézard, B., Vinatier, S., 2020. On the H$_2$ abundance and ortho-to-para ratio in Titan's troposphere. Icarus 344, 113261. http://dx.doi.org/10.1016/j.icarus.2019.03.038.

Bézard, B., Vinatier, S., Achterberg, R.K., 2018. Seasonal radiative modeling of Titan's stratospheric temperatures at low latitudes. Icarus 302, 437–450. http://dx.doi.org/10.1016/j.icarus.2017.11.034.

Borysow, A., Frommhold, L., 1986. Theoretical Collision-induced rototranslational absorption spectra for modeling Titan's atmosphere: H$_2$–N$_2$ pairs. Astrophys. J. 303, 495. http://dx.doi.org/10.1086/164096.

Bouanich, J.-P., Blanquet, G., Populaire, J.-C., Walrand, J., 1998. Nitrogen broadening of acetylene lines in the ν_5 band at low temperature. J. Molec. Spectrosc. 190 (1), 7–14. http://dx.doi.org/10.1006/jmsp.1998.7559.

Conrath, B.J., Gierasch, P.J., Ustinov, E.A., 1998. Thermal structure and para hydrogen fraction on the outer planets from voyager IRIS measurements. Icarus 135 (2), 501–517. http://dx.doi.org/10.1006/icar.1998.6000.

Courtin, R., Swinyard, B.M., Moreno, R., Fulton, T., Lellouch, E., Rengel, M., Hartogh, P., 2011. First results of Herschel-SPIRE observations of Titan. Astronom. Astrophys. 536, L2. http://dx.doi.org/10.1051/0004-6361/201118304.

Coustenis, A., Achterberg, R.K., Conrath, B.J., Jennings, D.E., Marten, A., Gautier, D., Nixon, C.A., Flasar, F.M., Teanby, N.A., Bézard, B., Samuelson, R.E., Carlson, R.C., Lellouch, E., Bjoraker, G.L., Romani, P.N., Taylor, F.W., Irwin, P.G.J., Fouchet, T., Hubert, A., Orton, G.S., Kunde, V.G., Vinatier, S., Mondellini, J., Abbas, M.M., Courtin, R., 2007. The composition of Titan's stratosphere from Cassini/CIRS midinfrared spectra. Icarus 189 (1), 35–62. http://dx.doi.org/10.1016/j.icarus.2006.12.022.

Coustenis, A., Bézard, B., Gautier, D., 1989. Titan's atmosphere from Voyager infrared observations. II. The CH$_3$D abundance and D/H ratio from the 900-1200 cm^{-1} spectral region. Icarus 82 (1), 67–80.

Coustenis, A., Jennings, D.E., Achterberg, R.K., Lavvas, P., Bampasidis, G., Nixon, C.A., Flasar, F.M., 2020. Titan's neutral atmosphere seasonal variations up to the end of the Cassini mission. Icarus 344, 113413. http://dx.doi.org/10.1016/j.icarus.2019.113413.

Coustenis, A., Jennings, D.E., Jolly, A., Bénilan, Y., Nixon, C.A., Vinatier, S., Gautier, D., Bjoraker, G.L., Romani, P.N., Carlson, R.C., Flasar, F.M., 2008. Detection of C_2HD and the D/H ratio on Titan. Icarus 197 (2), 539–548. http://dx.doi.org/10.1016/j.icarus.2008.06.003.

Coustenis, A., Salama, A., Schulz, B., Ott, S., Lellouch, E., Encrenaz, T., Gautier, D., Feuchtgruber, H., 2003. Titan's atmosphere from ISO mid-infrared spectroscopy. Icarus 161 (2), 383–403. http://dx.doi.org/10.1016/S0019-1035(02)00028-3.

de Bergh, C., Courtin, R., Bézard, B., Coustenis, A., Lellouch, E., Hirtzig, M., Rannou, P., Drossart, P., Campargue, A., Kassi, S., Wang, L., Boudon, V., Nikitin, A., Tyuterev, V., 2012. Applications of a new set of methane line parameters to the modeling of Titan's spectrum in the 1.58 μm window. Planet. Space Sci. 61 (1), 85–98. http://dx.doi.org/10.1016/j.pss.2011.05.003.

de Bergh, C., Lutz, B.L., Owen, T., Chauville, J., 1988. Monodeuterated methane in the outer solar system. Its abundance on Titan. Astrophys. J. 329, 951. http://dx.doi.org/10.1086/166439.

Delahaye, T., Armante, R., Scott, N.A., Jacquinet-Husson, N., Chédin, A., Crépeau, L., Crevoisier, C., Douet, V., Perrin, A., Barbe, A., Boudon, V., Campargue, A., Coudert, L.H., Ebert, V., Flaud, J.M., Gamache, R.R., Jacquemart, D., Jolly, A., Kwabia Tchana, F., Kyuberis, A., Li, G., Lyulin, O.M., Manceron, L., Mikhailenko, S., Moazzen-Ahmadi, N., Müller, H.S.P., Naumenko, O.V., Nikitin, A., Perevalov, V.I., Richard, C., Starikova, E., Tashkun, S.A., Tyuterev, V.G., Vander Auwera, J., Vispoel, B., Yachmenev, A., Yurchenko, S., 2021. The 2020 edition of the GEISA spectroscopic database. J. Mol. Spectrosc. 380, 111510. http://dx.doi.org/10.1016/j.jms.2021.111510.

Dobrijevic, M., Hébrard, E., Loison, J.C., Hickson, K.M., 2014. Coupling of oxygen, nitrogen, and hydrocarbon species in the photochemistry of Titan's atmosphere. Icarus 228, 324–346. http://dx.doi.org/10.1016/j.icarus.2013.10.015.

Dobrijevic, M., Loison, J.C., 2018. The photochemical fractionation of nitrogen isotopologues in Titan's atmosphere. Icarus 307, 371–379. http://dx.doi.org/10.1016/j.icarus.2017.10.027.

Dobrijevic, M., Loison, J.C., Hickson, K.M., Gronoff, G., 2016. 1D-coupled photochemical model of neutrals, cations and anions in the atmosphere of Titan. Icarus 268, 313–339. http://dx.doi.org/10.1016/j.icarus.2015.12.045.

Finenko, A.A., Bézard, B., Gordon, I.E., Chistikov, D.N., Lokshtanov, S.E., Petrov, S.V., Vigasin, A.A., 2022. Trajectory-based simulation of far-infrared collision-induced absorption profiles of CH_4-N_2 for modeling Titan's atmosphere. Astrophys. J. Suppl. S 258 (2), 33. http://dx.doi.org/10.3847/1538-4365/ac36d3.

Flasar, F.M., Kunde, V.G., Abbas, M.M., Achterberg, R.K., Ade, P., Barucci, A., Bézard, B., Bjoraker, G.L., Brasunas, J.C., Calcutt, S., Carlson, R., Césarsky, C.J., Conrath, B.J., Coradini, A., Courtin, R., Coustenis, A., Edberg, S., Edgington, S., Ferrari, C., Fouchet, T., Gautier, D., Gierasch, P.J., Grossman, K., Irwin, P., Jennings, D.E., Lellouch, E., Mamoutkine, A., Marten, A., Meyer, J.P., Nixon, C.A., Orton, G.S., Owen, T.C., Pearl, J.C., Prangé, R., Raulin, F., Read, P.L., Romani, P.N., Samuelson, R.E., Segura, M.E., Showalter, M.R., Simon-Miller, A.A., Smith, M.D., Spencer, J.R., Spilker, L.J., Taylor, F.W., 2004. Exploring the saturn system in the thermal infrared: The composite infrared spectrometer. Space Sci. Rev. 115 (1–4), 169–297. http://dx.doi.org/10.1007/s11214-004-1454-9.

Fulchignoni, M., Ferri, F., Angrilli, F., Ball, A.J., Bar-Nun, A., Barucci, M.A., Bettanini, C., Bianchini, G., Borucki, W., Colombatti, G., Coradini, M., Coustenis, A., Debei, S., Falkner, P., Fanti, G., Flamini, E., Gaborit, V., Grard, R., Hamelin, M., Harri, A.M., Hathi, B., Jernej, I., Leese, M.R., Lehto, A., Lion Stoppato, P.F., López-Moreno, J.J., Mäkinen, T., McDonnell, J.A.M., McKay, C.P., Molina-Cuberos, G., Neubauer, F.M., Pirronello, V., Rodrigo, R., Saggin, B., Schwingenschuh, K., Seiff, A., Simões, F., Svedhem, H., Tokano, T., Towner, M.C., Trautner, R., Withers, P., Zarnecki, J.C., 2005. In situ measurements of the physical characteristics of Titan's environment. Nature 438 (7069), 785–791. http://dx.doi.org/10.1038/nature04314.

Gurwell, M.A., 2004. Submillimeter observations of Titan: Global measures of stratospheric temperature, CO, HCN, HC_3N, and the isotopic ratios $^{12}C/^{13}C$ and $^{14}N/^{15}N$. Astrophys. J. Lett. 616 (1), L7–L10. http://dx.doi.org/10.1086/423954.

Jennings, D.E., Flasar, F.M., Kunde, V.G., Nixon, C.A., Segura, M.E., Romani, P.N., Gorius, N., Albright, S., Brasunas, J.C., Carlson, R.C., Mamoutkine, A.A., Guandique, E., Kaelberer, M.S., Aslam, S., Achterberg, R.K., Bjoraker, G.L., Anderson, C.M., Cottini, V., Pearl, J.C., Smith, M.D., Hesman, B.E., Barney, R.D., Calcutt, S., Vellacott, T.J., Spilker, L.J., Edgington, S.G., Brooks, S.M., Ade, P., Schinder, P.J., Coustenis, A., Courtin, R., Michel, G., Fettig, R., Pilorz, S., Ferrari, C., 2017. Composite infrared spectrometer (CIRS) on Cassini. Appl. Opt. 56 (18), 5274. http://dx.doi.org/10.1364/ao.56.005274.

Jolly, A., Benilan, Y., Cané, E., Fusina, L., Tamassia, F., Fayt, A., Robert, S., Herman, M., 2008. Measured integrated band intensities and simulated line-by-line spectra for $^{12}C_2HD$ between 25 and 2.5 μm, and new global vibration rotation parameters for the bending vibrations. J. Quant. Spectrosc. RA 109, 2846–2856. http://dx.doi.org/10.1016/j.jqsrt.2008.08.004.

Karman, T., Miliordos, E., Hunt, K.L.C., Groenenboom, G.C., van der Avoird, A., 2015. Quantum mechanical calculation of the collision-induced absorption spectra of N_2-N_2 with anisotropic interactions. J. Chem. Phys. 142 (8), 084306. http://dx.doi.org/10.1063/1.4907917.

Krasnopolsky, V.A., 2014. Chemical composition of Titan's atmosphere and ionosphere: Observations and the photochemical model. Icarus 236, 83–91. http://dx.doi.org/10.1016/j.icarus.2014.03.041.

Lacy, J.H., Richter, M.J., Greathouse, T.K., Jaffe, D.T., Zhu, Q., 2002. TEXES: A sensitive high-resolution grating spectrograph for the mid-infrared. Publ. Astron. Soc. Pac. 114 (792), 153–168. http://dx.doi.org/10.1086/338730.

Lara, L.M., Lellouch, E., González, M., Moreno, R., Rengel, M., 2014. A time-dependent photochemical model for Titan's atmosphere and the origin of H_2O. Astronom. Astrophys. 566, A143. http://dx.doi.org/10.1051/0004-6361/201323085.

Lebofsky, L., Spencer, J., 1989. Radiometry and thermal modeling of asteroids. In: Binzel, R., Gehrels, T., Matthews, M. (Eds.), Asteroids II. Univ. of Arizona Press, Tucson, pp. 128–147.

Lellouch, E., Bézard, B., Flasar, F.M., Vinatier, S., Achterberg, R., Nixon, C.A., Bjoraker, G.L., Gorius, N., 2014. The distribution of methane in Titan's stratosphere from Cassini/CIRS observations. Icarus 231, 323–337. http://dx.doi.org/10.1016/j.icarus.2013.12.016.

Lim, L.F., McConnochie, T.H., Bell, J.F., Hayward, T.L., 2005. Thermal infrared (8–13 μm) spectra of 29 asteroids: the Cornell mid-infrared asteroid spectroscopy (MIDAS) survey. Icarus 173 (2), 385–408. http://dx.doi.org/10.1016/j.icarus.2004.08.005.

Lombardo, N.A., Nixon, C.A., Greathouse, T.K., Bézard, B., Jolly, A., Vinatier, S., Teanby, N.A., Richter, M.J., Irwin, P.J.G., Coustenis, A., Flasar, F.M., 2019. Detection of propadiene on Titan. Astrophys. J. Lett. 881 (2), L33. http://dx.doi.org/10.3847/2041-8213/ab3860.

Lunine, J.I., Yung, Y.L., Lorenz, R.D., 1999. On the volatile inventory of Titan from isotopic abundances in nitrogen and methane. Planet. Space Sci. 47 (10–11), 1291–1303. http://dx.doi.org/10.1016/S0032-0633(99)00052-5.

Marten, A., Hidayat, T., Biraud, Y., Moreno, R., 2002. New millimeter heterodyne observations of Titan: Vertical distributions of nitriles HCN, HC_3N, CH_3CN, and the isotopic ratio $^{15}N/^{14}N$ in its atmosphere. Icarus 158 (2), 532–544. http://dx.doi.org/10.1006/icar.2002.6897.

Mathé, C., Vinatier, S., Bézard, B., Lebonnois, S., Gorius, N., Jennings, D.E., Mamoutkine, A., Guandique, E., Vatant d'Ollone, J., 2020. Seasonal changes in the middle atmosphere of Titan from Cassini/CIRS observations: Temperature and trace species abundance profiles from 2004 to 2017. Icarus 344, 113547. http://dx.doi.org/10.1016/j.icarus.2019.113547.

Moreno, R., Lellouch, E., Lara, L.M., Courtin, R., Bockelée-Morvan, D., Hartogh, P., Rengel, M., Biver, N., Banaszkiewicz, M., González, A., 2011. First detection of hydrogen isocyanide (HNC) in Titan's atmosphere. Astronom. Astrophys. 536, L12. http://dx.doi.org/10.1051/0004-6361/201118189.

Moreno, R., Lellouch, E., Lara, L.M., Feuchtgruber, H., Rengel, M., Hartogh, P., Courtin, R., 2012. The abundance, vertical distribution and origin of H_2O in Titan's atmosphere: Herschel observations and photochemical modelling. Icarus 221 (2), 753–767. http://dx.doi.org/10.1016/j.icarus.2012.09.006.

Niemann, H.B., Atreya, S.K., Demick, J.E., Gautier, D., Haberman, J.A., Harpold, D.N., Kasprzak, W.T., Lunine, J.I., Owen, T.C., Raulin, F., 2010. Composition of Titan's lower atmosphere and simple surface volatiles as measured by the Cassini-Huygens probe gas chromatograph mass spectrometer experiment. J. Geophys. Res. 115 (E12), E12006. http://dx.doi.org/10.1029/2010JE003659.

Nixon, C.A., Ansty, T.M., Lombardo, N.A., Bjoraker, G.L., Achterberg, R.K., Annex, A.M., Rice, M., Romani, P.N., Jennings, D.E., Samuelson, R.E., Anderson, C.M., Coustenis, A., Bézard, B., Vinatier, S., Lellouch, E., Courtin, R., Teanby, N.A., Cottini, V., Flasar, F.M., 2019. Cassini composite infrared spectrometer (CIRS) observations of Titan 2004–2017. Astrophys. J. Suppl. S 244 (1), 14. http://dx.doi.org/10.3847/1538-4365/ab3799.

Nixon, C.A., Temelso, B., Vinatier, S., Teanby, N.A., Bézard, B., Achterberg, R.K., Mandt, K.E., Sherrill, C.D., Irwin, P.G.J., Jennings, D.E., Romani, P.N., Coustenis, A., Flasar, F.M., 2012. Isotopic ratios in Titan's methane: Measurements and modeling. Astrophys. J. 749 (2), 159. http://dx.doi.org/10.1088/0004-637X/749/2/159.

Nixon, C.A., Thelen, A.E., Cordiner, M.A., Kisiel, Z., Charnley, S.B., Molter, E.M., Serigano, J., Irwin, P.G.J., Teanby, N.A., Kuan, Y.-J., 2020. Detection of cyclopropenylidene on Titan with ALMA. Astron. J. 160 (5), 205. http://dx.doi.org/10.3847/1538-3881/abb679.

Owen, T., Lutz, B.L., de Bergh, C., 1986. Deuterium in the outer Solar System: evidence for two distinct reservoirs. Nature 320 (6059), 244–246. http://dx.doi.org/10.1038/320244a0.

Penteado, P.F., Griffith, C.A., Greathouse, T.K., de Bergh, C., 2005. Measurements of CH_3D and CH_4 in Titan from infrared spectroscopy. Astrophys. J. Lett. 629 (1), L53–L56. http://dx.doi.org/10.1086/444353.

Pinto, J.P., Lunine, J.I., Kim, S.J., Yung, Y.L., 1986. D to H ratio and the origin and evolution of Titan's atmosphere. Nature 319 (6052), 388–390. http://dx.doi.org/10.1038/319388a0.

Rey, M., Nikitin, A.V., Bézard, B., Rannou, P., Coustenis, A., Tyuterev, V.G., 2018. New accurate theoretical line lists of $^{12}CH_4$ and $^{13}CH_4$ in the 0-13400 cm^{-1} range: Application to the modeling of methane absorption in Titan's atmosphere. Icarus 303, 114–130. http://dx.doi.org/10.1016/j.icarus.2017.12.045.

Thelen, A.E., Cordiner, M.A., Nixon, C.A., Vuitton, V., Kisiel, Z., Charnley, S.B., Palmer, M.Y., Teanby, N.A., Irwin, P.G.J., 2020. Detection of CH_3C_3N in Titan's atmosphere. Astrophys. J. Lett. 903 (1), L22. http://dx.doi.org/10.3847/2041-8213/abc1e1.

Tribbett, P.D., Robinson, T.D., Koskinen, T.T., 2021. Titan in transit: Ultraviolet stellar occultation observations reveal a complex atmospheric structure. Planet. Sci. J. 2 (3), 109. http://dx.doi.org/10.3847/PSJ/abf92d.

Vernazza, P., Ferrais, M., Jorda, L., Hanuš, J., Carry, B., Marsset, M., Brož, M., Fetick, R., Viikinkoski, M., Marchis, F., Vachier, F., Drouard, A., Fusco, T., Birlan, M., Podlewska-Gaca, E., Rambaux, N., Neveu, M., Bartczak, P., Dudziński, G., Jehin, E., Beck, P., Berthier, J., Castillo-Rogez, J., Cipriani, F., Colas, F., Dumas, C., Ďurech, J., Grice, J., Kaasalainen, M., Kryszczynska, A., Lamy, P., Le Coroller, H., Marciniak, A., Michalowski, T., Michel, P., Santana-Ros, T., Tanga, P., Vigan, A., Witasse, O., Yang, B., Antonini, P., Audejean, M., Aurard, P., Behrend, R., Benkhaldoun, Z., Bosch, J.M., Chapman, A., Dalmon, L., Fauvaud, S., Hamanowa, H., Hamanowa, H., His, J., Jones, A., Kim, D.H., Kim, M.J., Krajewski, J., Labrevoir, O., Leroy, A., Livet, F., Molina, D., Montaigut, R., Oey, J., Payre, N., Reddy, V., Sabin, P., Sanchez, A.G., Socha, L., 2021. VLT/SPHERE imaging survey of the largest main-belt asteroids: Final results and synthesis. Astronom. Astrophys. 654, A56. http://dx.doi.org/10.1051/0004-6361/202141781.

Vinatier, S., Bézard, B., Fouchet, T., Teanby, N.A., de Kok, R., Irwin, P.G.J., Conrath, B.J., Nixon, C.A., Romani, P.N., Flasar, F.M., Coustenis, A., 2007a. Vertical abundance profiles of hydrocarbons in Titan's atmosphere at 15°S and 80°N retrieved from Cassini/CIRS spectra. Icarus 188 (1), 120–138. http://dx.doi.org/10.1016/j.icarus.2006.10.031.

Vinatier, S., Bézard, B., Nixon, C.A., 2007b. The Titan ^{14}N/^{15}N and ^{12}C/^{13}C isotopic ratios in HCN from Cassini/CIRS. Icarus 191 (2), 712–721. http://dx.doi.org/10.1016/j.icarus.2007.06.001.

Vinatier, S., Mathé, C., Bézard, B., Vatant d'Ollone, J., Lebonnois, S., Dauphin, C., Flasar, F.M., Achterberg, R.K., Seignovert, B., Sylvestre, M., Teanby, N.A., Gorius, N., Mamoutkine, A., Guandique, E., Jennings, D.E., 2020. Temperature and chemical species distributions in the middle atmosphere observed during Titan's late northern spring to early summer. Astronom. Astrophys. 641, A116. http://dx.doi.org/10.1051/0004-6361/202038411.

Vinatier, S., Rannou, P., Anderson, C.M., Bézard, B., de Kok, R., Samuelson, R.E., 2012. Optical constants of Titan's stratospheric aerosols in the 70-1500 cm^{-1} spectral range constrained by Cassini/CIRS observations. Icarus 219 (1), 5–12. http://dx.doi.org/10.1016/j.icarus.2012.02.009.

Vuitton, V., Yelle, R.V., Klippenstein, S.J., Hörst, S.M., Lavvas, P., 2019. Simulating the density of organic species in the atmosphere of Titan with a coupled ion-neutral photochemical model. Icarus 324, 120–197. http://dx.doi.org/10.1016/j.icarus.2018.06.013.